A New 2D Magnetic Induction Tomography System for Phantom Detection and Localization in Medical Applications

B. Gowry, Abu B. Shahriman, and Z. Zulkarnay

***Abstract*— Here we describe a new cost-effective magnetic induction tomography (MIT) system to identify and localize phantoms in biological tissues. The proposed 2D (two-dimensional) numerical simulation detection system consists of 8 transceiver coils. During the simulation process, one of the eight transceivers acts as a transmitter, and the rest act as receivers, thereby yielding 7 receiver readings. This process was repeated, and 56 (8 transmitters x 7 receivers) induced voltage readings (receiver readings) were obtained by activating different transceivers at a time. The induced voltage readings were then used to reconstruct the images of biological samples using a linear back-projection (LBP) algorithm. To assess the quality of the images, 10 frequency-based features and seven image-based features were extracted from the reconstructed images. Artificial neural network (ANN) and extreme learning machine (ELM) classifiers were used to distinguish the presence and locations of phantoms. The proposed method attained best accuracies of 91.90% (ELM) and 100% (ANN) for frequency features. The obtained results indicate that the proposed MIT design and features provide a promising alternative to detect and localize pathological conditions in the biological tissue.**

***Index Term*— ANN, biological tissue, ELM, LBP, magnetic induction tomography, numerical simulations.**

I. Introduction

Detection of early breast cancer in surrounding normal tissue can be challenging, but detection is essential to determine the subsequent treatment procedures. The physical basis of magnetic induction is being profited to propose novel diagnostic techniques for tumor detections in organs, but with challenges that need to be overcome. Moreover, its reliability and feasibility is still in the focus of many controversies as there are only a few extensive researches that have been conducted to date. Early detection of breast cancer is done by X-ray Mammography, which is also presently referred to as the gold standard modality by many healthcare institutes. Nevertheless, it is not very accurate and safe as it is unable to distinguish benign and malignant lesions due to their morphological similarities, its reduced sensitivity with age, its radiation hazards plus, its reduced efficiency in diagnosing cancer in patients with denser breast tissues. On top of that, almost 80% of the positive breast cancer cases diagnosed by this modality are negative when malignancy of the tumors is further investigated during biopsy. However, a better pre-biopsy technique should be introduced as biopsy procedures can be both physically and mentally painful. On the other hand, ultrasound is currently used to differentiate cystic and non-cystic growths as it is known for a number of advantages over other imaging modalities that is, it is safe and thereby is suitable for repetitive scanning, painless, and aids in needle biopsy. Despite its noble features, ultrasound still lacks in the sense that it is not efficient in imaging microcalifications that are the prognostic indicators of breast cancer. Breast Magnetic Resonance Imaging (MRI) though of high sensitivity is expensive and thus can be used only under certain clinical circumstances which are mainly for patients with implants or suspected multifocal carcinoma. Nuclear medicine, Microwave imaging [1], MRI based Elastography [2], Thermography [3], and Optical Mammography [4] 's potential in this area have also been discovered but with limited success [5]. In another study, mastectomy, which is the surgical removal of partial/entire breasts, ligature which is commonly known as sutures and cautery that is an agent to burn, sear or destroy abnormal tissues by means of injection of electric current or burning or laser are other techniques used which causes pain that is rather excruciating. Hence, X-ray Mammography still remains as the primary method of diagnosis [6].

New techniques which have the potential to overcome the limitations of the conventional gold standard breast cancer imaging modality rely upon the prominent changes seen in the electrical properties and subsequently the electrical impedance of breast tissues due to the presence of high vasculature during the development of malignancies [7]. This has suggested the Electrical Impedance Tomography (EIT) which injects a considerably small amount of alternating current into the body through a set of electrode arrays to measure sub sensory voltages [8]. However, the plunged accuracies in EIT are errors brought in by poor skin to electrode contact, failure to know the exact location of electrodes due to human body surface variability, and the certain highly sensitive parts of the body [9]. Hence, a technique proposed to replace the electrode dependent measurements would be the contactless MIT

Here we describe a new cost-effective MIT system to identify and localize phantoms in biological tissues. In this study, the biological tissue and phantom has the di-electrical properties of normal breast and tumor tissue, respectively. The estimations of the conductivity and permittivity of the typical human breast and tumor tissue are taken from the study conducted by D. A. Francis in [7],[10]. The proposed 2D

All of the authors are with School of Mechatronic Engineering, Universiti Malaysia Perlis, Pauh Putra Campus, 02600 Arau, Perlis, Malaysia, (e-mail: gowry@studentmail.unimap.edu.my).

numerical simulation detection system consists of 8 transceiver coils. During the simulation process, one of the eight transceivers acts as a transmitter, and the rest act as receivers, thereby yielding 7 receiver readings. This process was repeated and 56 (8 transmitters x 7 receivers) induced voltage readings (receiver readings) were obtained by activating different transceivers at a time. The induced voltage readings were then used to reconstruct the images of biological samples using a LBP algorithm. There are numerous image reconstruction algorithms, for example, linear back-projection, nonlinear algorithms, and filtered back projection; however, in this article, only LBP algorithm is utilized as it has become a well-known technique among analysts due to its low computation requirements and its basic and quick response as an algorithm. To assess the quality of the images, 10 frequency-based features and seven image-based features were extracted from the reconstructed images. ANN and ELM classifiers were used to distinguish the presence and locations of phantoms. A multilayer perceptron network (or ANN) is a supervised machine learning algorithm that is able to classify given inputs into one or several numbers of possible outputs or classes. In previous years, the ELM technique has been widely used for machine learning and artificial intelligence because of its remarkable qualities (i.e. its quick training ability, great generalization, and global classification potential). ELM is a successful answer for the single hidden layer feed forward systems (SLFNs), and has been shown to have fantastic learning precision/speed in different applications, for example, face grouping, image segmentation, and human activity recognition [11]. Not at all like the other conventional learning algorithms, e.g. back propagation (BP)-based neural networks (NNs) or support vector machine (SVM), the parameters of concealed layers of the ELM are arbitrarily created and do not need to be tuned. In other words, the hidden layer could be built up before the training samples are obtained.

The proposed method attained best accuracies of 91.90% (ELM) and 100% (ANN) for frequency features. The obtained results indicate that the proposed MIT design and features provide a promising alternative to detect and localize pathological conditions in the biological tissue.

II. THE HISTORY OF MAGNETIC INDUCTION BASED TECHNOLOGIES

In 2009, low-frequency, sub-surface imaging of biological tissue was accomplished. The measurement of the output magnetic field was done at 50 kHz by scanning the body surface where each transmitter provides a sample that is later averaged and used with the steepest descent algorithm for visualization [12]. Electromagnetic properties (EMP) were further investigated in [13], where the EMP of biological tissues, which were taken from the breast, rectum, and ovary, were determined with the help of bio-impedance measurements using Agilent 4294A precision impedance analyzer, PC, power supply block, and text fixtures by Marinovaet al. Impedance amplitude and phase angle were measured using an auto-balancing bridge method and visualized for the 100 Hz to 10 MHz frequency range. Among the preliminary results of the proposed system is its high conductivity value for normal tissues of breast and rectum, particularly at frequencies from 100 Hz to 10 kHz. As for the ovary tissue, the tumor tissue illustrated a higher conductivity throughout the frequency range of the study [13].

Meanwhile, Barai et al. mentioned in their work that the reconstruction of conductivity values that vary with a certain frequency limit is the definition of electrical bio-impedance spectroscopy (BIS). The only difference of BIS with MIT is that it operates in a unique contactless environment with the biological structure. A quasi-static approximation was made in this study, while experiments were conducted with saline, yeast suspensions, solid bio-tissues like potatoes and ripening of banana at 200 kHz to 20 MHz. The advantages of the system are that the sensors can be isolated from any extreme environment, and the sensors are able to operate with an air gap between them. Also, only easily available insulating materials are needed, and the system accuracy increases proportionally with frequency at a data acquisition time of merely 52 s. However, very small induced current densities and their strong dependencies with frequency that restricts SNR at low frequencies are among the system's drawbacks [14].

In 2012, a review on the advancement of transmitter and receiver sensors for use in biomedical area for MIT was performed. The entire process of MIT begins with the exertion of a magnetic field through a coil around a biological sample where the transmitted magnetic field, which is also referred to as the primary field (*B*), then induces an eddy current density in the sample, creating a new secondary field ($B+\Delta B$). The secondary field can be observed from a similar coil (receiver coil) placed at a certain distance away from the first coil. Unlike EIT, MIT is not only a non-invasive technique, but it also does not require any contact with the patient for image reconstruction purposes, thereby eliminating the old-fashioned skin-electrode impedance problem. However, the MIT is prone to be affected by drastic primary fields and noise; in particular, biological tissues are known for its very poor conductivity. These issues are currently being curbed by improvising the design of both the transmitting and receiving sensors by means of the introduction of screen-coupled excitatory coils, incorporation of gradiometers, as well as selection of highly sensitive sensors at the receiver's end [9].

By the end of 2013, studies focused on magnetic resonance driven impedance tomography (MRDEIT), which is the reconstruction of tissue conductivity profile by firstly exerting magnetic field to model the induced current density and then measuring the voltage drop from surface electrodes. The MRDEIT signal is the result of magnetization, Mo , which revolves in the transverse plane perpendicular to the $Bo(z)$ direction at echo time (T_E) once the RF excitation pulse has been omitted during a typical cycle of a MR sequence. MRDEIT imaging can be done via either the forward (known electrical properties and unknown voltage drop) method or the inverse method. A 12 cm * 12 cm * 12 cm acrylic cube and cylindrical glass bottle as well as a 25 * 25 * 25 sized brick

finite element mesh and a cylindrical shaped geometry was used for the experimental and phantom simulation, respectively, to represent the normal and lesion tissues. The lesion was modeled to have twice the conductivity of the baseline. The advantage of the system is that the contrast between healthy and unhealthy tissues was discernible for a maximum noise level of 10% while involving no electric current injection. Among the drawbacks are the presence of a significant amount of noise and artifacts near the central region of lesions [15].

A magnetic induction spectroscopy (MIS) strategy was then further investigated and created towards identifying pathological conditions, the identification of volumetric brain edema, a state of gathered liquid substance in cerebrum tissues through an inductive phase shift that was considered in [16]. In a past study done in 2007, the lung, muscle, and cerebrum tissue conduct was observed to be correlated with the inductive phase shift. The whole framework was made of a circular disc of tissue set in the middle of two coils. The outcomes demonstrated a huge phase shift and edema connection proof at frequencies of more than 10 MHz [17]. Gonzalez et al. examined the innovation and after-effects of a pilot study directed on volumetric electromagnetic phase-shift spectroscopy (VEPS) in distinguishing edema and hematoma. VEPS demonstrated $p\langle 0.05$ for distinguishing the normal and damaged brain tissues, in addition to recognizing cerebrum edema and hematoma [18].

Chronic cerebral hemorrhage (CCH), which is extreme seeping in cerebrum tissues, was observed by J. Sun et al. in rabbits by noting the alterations in the inductive phase shift as opposed to the costly conventional MRI and Positron Emission Tomography (PET) machines. In [19]-[20], acute cerebral hemorrhage (ACH), that is, the unconstrained seeping in cerebrum tissues without the vicinity of injury, was observed in an ongoing manner by means of animal analysis, utilizing customized magnetic induction phase shift (MIPS) device to demonstrate the relationship between intracranial pressure (ICP), MIPS, and draining volume. ICP and the pulse were initially observed in an hourly interval at 10.7 MHz. The principal attainability investigation of MIS and ischemia and human breast cancer was later performed by González et al. [21],[8],[7]. In [22], our team has made a comparative study with [7] to detect breast cancer using MIS technique and concluded that our proposed coil configuration has a higher inductive phase shift intensity which denotes the presence and absence of a breast tumor.

Later in 2015, the hybrid combination of computer simulation technology (CST) for simulation, and Matlab for classification of the simulation outcome purposes proved the ability of the microwave imaging technique for the detection and localization of breast lesions. The proposed method depends on the utilization of a customized neural network model (ANN) [23]-[24]. Although the practical motivation is similar to our proposed method that is for tumor detection, studies conducted in [23]-[24] used a 3D (three –dimensional) simulation phantom and a different material database corresponding to the microwave frequency range. An extremely hopeful result, that is, a classification accuracy of 94.4%, has been achieved for the initial part of the received antenna signals with the ANN model [23]. From the literature, it can be seen that the benefits of magnetic induction techniques are being progressively explored in the medical field. However, the performance of magnetic induction-based modality cannot be directly compared with the existing real-time imaging modalities like X-ray, ultrasound, and MRI as they are of one-dimensional data. Motivated by the work done in [7],[23], our team has proposed a new method for imaging abnormalities or pathological conditions in biological tissues using two well-known classifiers. This study is an extension of our work in [22] using a higher number of transceivers for tissue imaging purposes. Figure 1 shows the flow chart of the simulation work done in this paper.

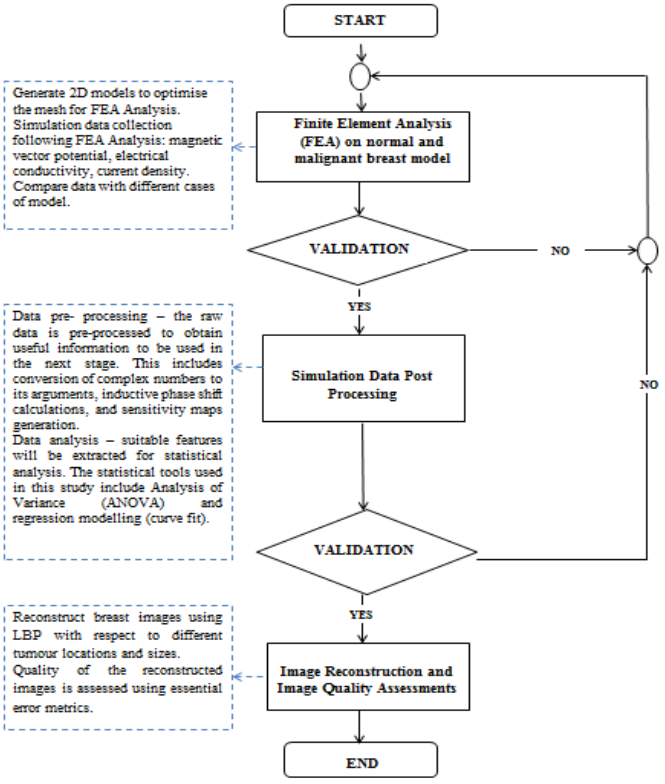

Fig. 1. Flow chart of the methodology.

III. Numerical Simulation Method 2D MIT System Configuration And Magnetic Induction Concept

A. *Numerical Simulation Model*

In this study, the biological tissue and phantom has the di-electrical properties of normal breast and tumor tissue, respectively. The simulation model consists of 8 transceiver sensor coils (circles) with 1 coil acting as the transmitter (excited by 1 A) and the rest acting as receivers at a single time period. The rectangle speaks to the insulator (i.e., air), while the greater and smaller circles represent the biological tissue and phantom individually (refer to Fig.1).

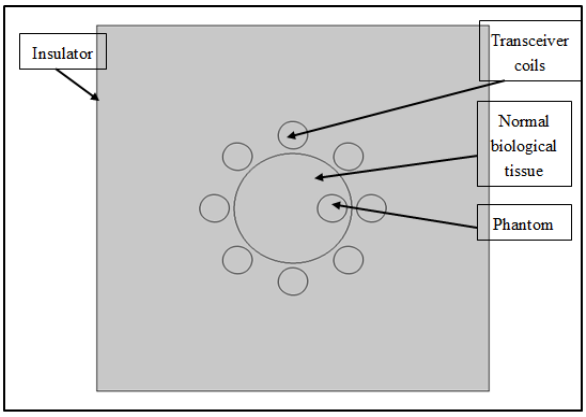

Fig. 1. 2D MIT system and biological tissue model.

B. Finite Element Method and Simulation Criteria

The workstation used for the reenactment works comprises of a Dell Inspiron PC with an i5 processor and 8GB RAM. In Comsol, a triangular cross section with a linear and iterative solver was utilized. The default solver relative resilience is 0.001. Table 1 presents the parameters included in the study. The estimations of the conductivity and permittivity of the typical human breast and tumor tissue are taken from [7]. The 10 MHz frequency, with which the simulations are led, is purposely chosen to be in the β scattering locale where most pathological changes occur [25]. In the meantime, a time harmonic and quasi-static assumption, (1), was additionally made in the Ampere's equation utilized in Comsol to produce the magnetic vector potential appropriation in the model. As such, the displacement current streams in the Ampere's mathematical statement were disregarded, and a non-moving geometry was considered with no outside electric potential gradient.

$$(\sigma j\omega - \omega^2\varepsilon)A + \nabla \times (\mu^{-1}(\nabla \times A)) = J_e \quad (1)$$

where μ is the medium permeability (henry/meter) and ε is the medium permittivity (farad/meter), σ is the medium conductivity (siemens/meter), ω is the angular frequency, J_e is the external electric current density (ampere/ meter ^{2}), and A is the magnetic vector potential ($\vec{A}$).

TABLE I
LIST OF PARAMETERS OF 2D MIT SIMULATION MODEL

Parameters	Values
Number of turns of coils	5
Current applied at coils	Excitation coil: 1 A Detecting coil: 0 A
Coil type	Linear
Coil material	Copper
Diameter of coils	0.015 m
Diameter of normal tissue	0.06 m
Diameter of phantom	0.015 m
Size of insulator	0.4 m * 0.4 m
Frequency used	10 MHz
Di-electrical properties of the biological tissue/breast	Conductivity: 3.2 mS/m Permittivity: 12
Di-electrical properties of the phantom/tumor	Conductivity: 8.2 mS/m Permittivity: 300

C. Magnetic Induction Concept

The phantom of the biological tissue could be distinguished using magnetic affectation when electrical waves are transmitted to one of the sensor coils (transmitter) of the tomography framework, producing an attractive field around the coil as per the Ampere's law (refer to Fig.2). This attractive magnetic field when going through the biological tissue and phantom thus impels the perturbed eddy current present as an element of di-electrical properties that exist in them and also in the rest of the sensor coils (receivers), restricting the change that is brought on it. This complies with Lenz's and Faraday's law of induction, (2):

$$\varepsilon = -\frac{\partial \phi}{\partial t} \quad (2)$$

where ε is the induced voltage, the negative sign signifies the direction, and $\partial\phi$ is the adjustment in the magnetic flux created.

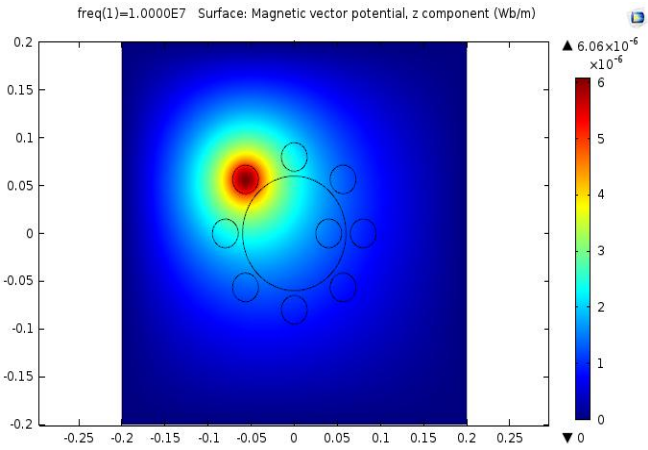

Fig. 2. Simulation output resulting from excitation of the 8th sensor.

The subsequent magnetic vector potential, which indicates the presence and absence of a phantom, depends on the distinction in the power of the induced voltage identified at the receiving coils. In Comsol, the induced voltage is evaluated by performing a surface integration of the product of the current density and magnetic vector potential at the receiver coils utilizing the mathematical statement given as part of [26], (3):

$$V_{mn} = -j\omega \int_{\Omega_c} A_{\bullet} J_0 dS \tag{3}$$

where A and J_0 are the magnetic vector potential and current density passing through the coil respectively.

IV. Image Reconstruction

A. Sensitivity Matrix Calculation

The sensitivity grid map for a given sensor setup is an essential step in the inverse part of every forward simulation problem. The sensitivity matrix, *S*, shapes a premise set from which image vectors can be acquired [27]-[28]. Fundamentally, every pixel of S speaks to the effect of the sensor framework to every conductivity pixel in a uniform distribution of sample [29]:

$$S = \frac{\partial V_{mn}}{\partial \sigma_k} = -\omega^2 \frac{\int_{\Omega_k} A_m \cdot A_n \partial v}{I_0} \tag{4}$$

where V_{mn} is the voltage reading, σ_k is the conductivity of pixel *k*, Ω_k is the area of the perturbation *k*, A_m and A_n are magnetic vector potential solutions when the excitation coil m is excited by I_0 and when the sensing coil n is excited with unit current, respectively.

The sensitivity matrix is carefully construed in accordance to (4) and is then generated in MATLAB; refer to Fig.3. The following are the procedures to construct a single sensitivity map:

Step 1: Excite every sensor one at a time, and store the resulting Comsol simulation data of magnetic vector potential in the form of a 128*128 pixel grid. The arguments of the complex magnetic vector potential are obtained using the equation provided in [8].

Step 2: Compute the dot product of the magnetic vector potential maps for each and every transceiver pair (Total number of pairs: 8 transmitters * 7 receivers = 56 matrix).

Step 3: Sum all the matrix generated in Step 2. The final matrix is called the weight balance map (WBM).

Step 4: Normalize each sensitivity matrix (matrices generated in Step 2) by dividing it by the WBM.

B. Image Reconstruction Algorithm

The LBP calculation is based on the product of multiple matrices. Keeping in mind that the end goal is to reproduce the forward solution, each sensitivity map is multiplied by the corresponding sensor reading and summed. Although LBP produces blurred images with artifacts and 1/r image roll offs, it is still the fastest compared to other more accurate techniques[30]. The mathematical equation of LBP is stated in (5).

$$V_{LBP}(x,y) = \sum_{Tx=0}^{8} \sum_{Rx=0}^{7} S_{Tx,Rx} X\overline{M}_{Tx,Rx}(x,y) \tag{5}$$

where $V_{LBP}(x,y)$ is the voltage distribution obtained using LBP algorithm in n x n matrix where n is equals to dimension of sensitivity maps, $\overline{M}_{Tx,Rx}(x,y)$ is the induced voltage in Rx-th sensor coil for Tx-th projection, $S_{Tx,Rx}$ is the normalized sensitivity matrices for the view of Tx-Rx.

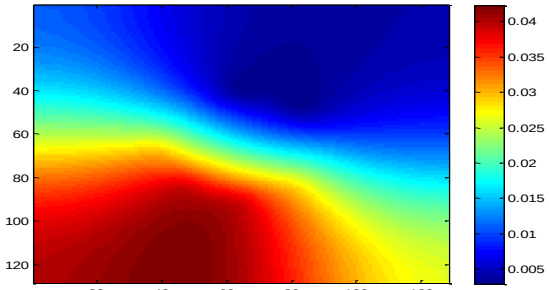

(a)

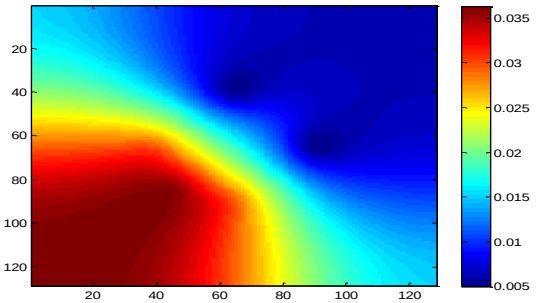

(b)

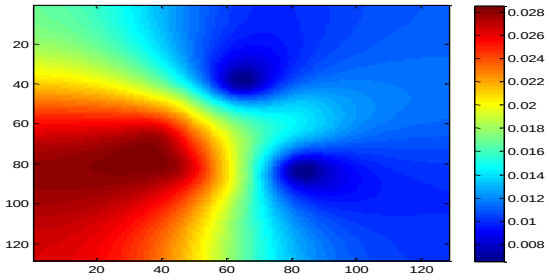

(c)

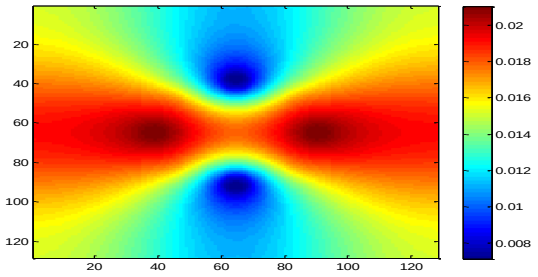

(d)

Fig. 3. Sensitivity maps of transmitter 1 with corresponding receivers ; (a) Receiver 1, (b) Receiver 2, (c) Receiver 3, (d) Receiver 4.

V. Construction of Classifiers

A. Data Acquisition

The data acquisition process is described below:

1. Place 8 sensor coils (circles) around the tissue model at an interval angle of 45 degrees;
2. Place a phantom at any quadrant in the model;
3. Transmit a 1 A random sinusoidal current in one of the sensor coils;
4. Obtain the induced voltage reading from the rest of the sensor coils;
5. Reconstruct the image of the simulation results;
6. Change the tumor position/quadrant, and rehash the strides (3-5).

The biological tissue was partitioned into four quadrants, and the phantom position was shifted 68 times (17 positions at every quadrant). The size of the field of view would be the size of the modeled biological tissue sample. In this manner, an aggregate of 70 images were created from the simulation results, which are composed of 2 images of the typical biological tissue without the existence of phantoms. Every image contains 128 * 128 pixels. The acquired images were then segmented for further processing of just the tissue region. The subsequent images consisted of 51 * 51 pixels.

B. Feature Extraction

A total of 17 features were extracted following analysis of variance (ANOVA) analysis. ANOVA is an extension of the *t* and *z*-test, which is a statistical method for analysis of variance. The *t*-test, however, cannot be used in this study as it is not applicable for more than two groups. In this work, this analysis is done to obtain the statistical significance of the features, and the resulting 17 significant features are described in the following sections. The features are grouped into two sets, namely, frequency domain features [31] and image based features taken from [32]- [33].

1) Set 1 (Frequency domain features)

a. Mean Frequency

It is an average frequency that is calculated by summing the product of image power spectrum and the frequency, and then dividing it by the total sum of spectrum density.

$$\text{MNF} = \sum_{j=1}^{M} f_j P_j \Big/ \sum_{j=1}^{M} P_j \tag{6}$$

where f_j is the frequency of the spectrum at frequency bin, j, P_j is the image power spectrum at frequency bin j, and M is the frequency bin length.

b. Mean power

It is an average power of the image vector power spectrum.

$$\text{MNP} = \sum_{j=1}^{M} P_j \Big/ M \tag{7}$$

c. Total power

TTP is the aggregate of the image vector power spectrum, also known as zero spectral moment ($SM0$).

$$\text{TTP} = \sum_{j=1}^{M} P_j = SM0 \tag{8}$$

d. Median Frequency

MDF is TTP feature divided by two.

$$\text{MDF} = \sum_{j=MDF}^{M} P_j = \frac{1}{2}\sum_{j=1}^{M} P_j \tag{9}$$

e. Peak frequency

It is the frequency when the power is at its maximum.

$$\text{PKF} = \max(P_j),\ j = 1,....M. \tag{10}$$

f. Power spectrum ratio

It is the ratio between the energy, P_0 which is nearby the maximum value of the image power spectrum and total power spectrum energy, *P*.

$$\text{PSR} = \frac{P_0}{P} = \sum_{j=f_0-n}^{f_0+n} P_j \Big/ \sum_{j=-\infty}^{\infty} P_j \tag{11}$$

where f_0 is a feature value of the PKF and *n* is the integral limit.

g. The 1st,2nd and 3rd spectral moments (SM1,SM2,SM3)

Another way to perform a statistical analysis to extract features from the image power spectrum is by using spectral moments. The most significant spectral moments are the first three.

$$SM = \sum_{j=1}^{M} P_j a \tag{12}$$

where $a = f_j$ for SM1, $a = f_j{}^2$ for SM2, and $a = f_j{}^3$ for SM3.

h. Relative Power Grading

$$\text{RPG} = \frac{P_{0(i)}}{P} \tag{13}$$

where energy $P_{0(i)}$ is a value that is nearby the maximum value of the image power spectrum for class *i* and the energy *P* is the individual energies of the image power spectrum for class *i*.

2) Set 2 (Image based features)

a. *Energy*

It is also known as the measure of uniformity.

$$\text{E} = \sum_i \sum_j p(i,j)^2 \tag{14}$$

where $p(i,j)$ is the $(i,j)^{th}$ pixel value of the image.

b. *Sum*

$$\text{S} = \sum_i \sum_j p(i,j) \tag{15}$$

c. Mean

$$\text{M} = \frac{1}{N^2} \sum_{i=1}^{N} \sum_{j=1}^{N} p(i,j) \tag{16}$$

where N is the total number of pixels in the image.

d. Standard deviation

$$\text{SD} = \sqrt{\frac{\sum\sum (p(i,j) - M)^2}{N^2}} \tag{17}$$

e. Inverse difference moment

It is the local homogeneity and is high when inverse gray level of the image pixels is high and local gray level is consistent.

$$\text{IDV} = \sum_i \sum_j \frac{p(i,j)}{1 + |i-j|} \tag{18}$$

f. Entropy

It measures the amount of signal loss during transmission and also contains the information of an image.

$$\text{EN} = -\sum_i \sum_j p(i,j) \log(p(i,j)) \tag{19}$$

g. Homogeneity

It is a quantity that increases with lesser contrast in the image.

$$\text{H} = \sum_i \sum_j \frac{p(i,j)}{1 + |i-j|^2} \tag{20}$$

C. Classification

1) ELM

ELM is a single hidden layer feed forward system where its weight parameters of hidden layers are randomly created and never updated [34]. The simplest form of the ELM training algorithm is as follows

$$\hat{Y} = W_2 \sigma(W_1 x) \tag{21}$$

where W_1 is the matrix of input-to-hidden-layer weights, σ is some activation function, and W_2 is the matrix of hidden-to-output-layer weights. The algorithm proceeds as follows:

1. Fill W_1 with Gaussian random noise;
2. Estimate W_2 by least-squares fit to a matrix of response variables Y, computed using the pseudo inverse $\cdot^+$, given a design matrix X:

$$W_2 = \sigma(W_1 X)^+ Y \tag{22}$$

2) ANN

ANN is a supervised machine learning algorithm that is able to classify given inputs into one or several numbers of possible outputs or classes. Unlike ELM, the ANN weights are updated for every iteration. In this work, we have a total of 70 samples, 17 input neurons, and 5 output neurons (Refer Table 2). The results are obtained by varying the number of hidden neurons, interchanging the input and hidden neuron activation functions, and varying the proportion of samples used for training, testing, and validation purposes.

TABLE II
ANN PARAMETERS

Parameters	**Calculations**
No of input samples	(4 quadrants * 17 phantom positions) + 2 normal biological tissue = 70 samples
No of input neurons	10 frequency domain features + 7 image based features = 17 input neurons
No of output neurons	Tissue with phantom at 4 different quadrants + 1 normal tissue without phantom = 5 output neurons
Transfer functions	Tansig, Purelin
Training function	trainlm

3) Dataset partitioning

For the identification and localization of a phantom in 2D, we utilized the steps given in section 5.1. The methodology for data acquisition was performed for 68 unique areas by uprooting the phantom inside each and every quadrant. Hence, a tissue model without existence of a phantom was utilized twice to obtain a typical healthy tissue image. The training and testing batch of the classifiers are as follows:

Batch (1): 70% of the dataset for each quadrant containing a phantom and 1 without the presence of a phantom were randomly utilized for learning the phase;

Batch (2): 30% of the dataset for each quadrant containing phantom and 1 without the presence of a phantom were randomly utilized for the test period.

VI. Results and Discussion

A. 2D MIT Images

Fig. 4 shows the images reconstructed by using a LBP algorithm and Comsol simulations of the proposed 2D MIT system. Three different images of the biological tissue with the phantom placed exactly at the center of the circular biological tissue (0,0), at the right most (0.04,0), and at the left most (-0.04,0) positions are shown. The image of a typical biological tissue with the absence of any phantoms is also shown as a reference image. Each figure contains the segmented image of the biological tissue only.

From the figure, all of the images show clear distinctions between one another, although the images appear to be blurred due to low number of sensors used unlike in the conventional MIT [9],[26],[30]. This helps to reduce the cost (i.e., maintenance and production cost) and computational time (i.e., scan time) of the system. Collectively, whenever there is a phantom present, there is a peak voltage, and its intensity depends on the phantom's distance from the transmitting sensor coils. 2.10 mV, 2.08 mV, and 2.08 mV peaks are reflected for the phantom positioned at the center and left and right ends of the tissue, respectively. The voltage peak of the phantom is highest when it is at the center as it is located furthest from the sensors, and thus the induced current density is the highest. Meanwhile, when there is no phantom present, a peak of 1.72 mV is shown in the middle of the tissue where the depth is highest. This could be explained by the Biot-Savart Law, which relates magnetic fields to the electrical current streams that are their sources. Electric current in a round circle makes an attractive magnetic field, which is more packed in the inside and along the z-axis of the circle [8].

To further strengthen the findings and to assess the quality of the images, classification results of the images are discussed in the following section.

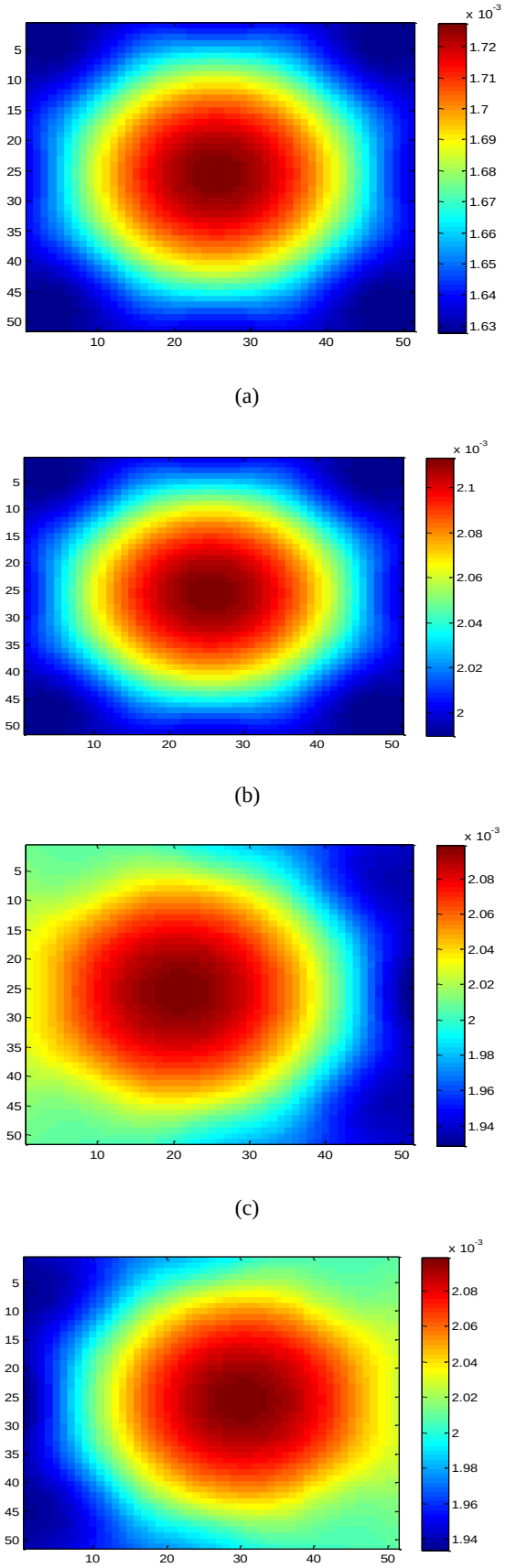

Fig. 4. Images reconstructed by using LBP algorithm; (a) Normal tissue, (b) Phantom at center. (c) Phantom at left, (d) Phantom at right.

B. *Classification Results*

TABLE III
CLASSIFICATION ACCURACIES OF DETECTION AND LOCALIZATION OF PHANTOMS WITH THE PROPOSED MIT IMAGING SYSTEM

	Set 1		Set 2		Set 3	
No. of Trials	ELM (%)	ANN (%)	ELM (%)	ANN (%)	ELM (%)	ANN (%)
1	80.95	100	28.57	75.7	90.48	98.6
2	85.71	100	26.9	74.3	90.48	97.1
3	100	100	30.3	74.3	95.24	74.3
4	95.24	100	40.6	74.3	95.24	100
5	100	100	26.9	74.3	95.24	74.3
6	85.71	100	20.9	74.3	95.24	74.3
7	95.24	100	44.6	74.3	95.24	72.9
8	95.24	100	22.5	75.7	90.48	75.7
9	80.95	100	28.2	74.3	95.24	98.6
10	100	100	36.8	74.3	100	74.3
Average	**91.90**	**100**	**30.62**	**74.58**	**94.28**	**84.01**

Table 3 shows the classification accuracies of ELM and ANN for 3 sets of features. Set 1 contains the frequency domain features, Set 2 contains the image based features, and Set 3 is the combination of Set 1 and Set 2 features. From the table, it can be deduced that the highest classification accuracy is attained by the ANN classifier with 100% accuracy using only frequency domain features. The performance of the proposed method is also better than in [23] that used microwave imaging technique, which is also an upcoming imaging technique for the detection of breast tumors. This proves that the proposed system is capable of not only detecting the presence of phantom in a biological tissue but also to tell its location, in this case, among the four quadrants.

VII. CONCLUSION

This work describes a new 2D MIT system with 8 sensor coils for the detection and localization of a phantom in biological tissue. Upon completing the simulation experiments, images of the simulation results were reconstructed using LBP. Three sets of features were extracted from the images: Set 1 contains ten frequency domain features; Set 2 contains seven image based features; and Set 3 contains combination of Set 1 and Set 2 features. The classifiers used were ELM and ANN. Based on the results, it can be concluded that the proposed system can effectively identify and localize phantoms in biological tissue. Since the proposed system is a new method for detecting phantoms in biological tissue, direct comparison with published works in the literature could not be made. The contactless environment with the sample is the primary nature of the proposed system that made it outperform other upcoming techniques like microwave and electrical impedance techniques. This nature would prevent physical trauma on the sample, which can be real human patients in the near future; also, it can reduce the unnecessary cost of operation on the shielding material that is to be placed between the sample and the system. Further study will be focused on creating a more realistic 3D MIT system as well as using healthy and pathological (e.g., cancer) human tissues or organ models.

ACKNOWLEDGMENT

The authors are highly indebted to Universiti Malaysia Perlis (Unimap) for their kind co-operation and encouragement which greatly assisted in the research work.

REFERENCES

[1] M. A. Fear, E. C., Hagness, S. C., Meaney, P. M., Okoniewski, and M.Stuchly, "Enhancing breast tumor detection with near-field imaging," *IEEE Microw. Mag.*, vol. 3, pp. 48–56, 2002.

[2] J. Van Houten, E. E. W., Doyley, M. M., Kennedy, F. E., Weaver and K. D. B., and Paulsen, "Initial in vivo experience with steady-state subzone-based MR Elastography of the human breast," *J Magn Reson Imaging*, vol. 17, pp. 72–85, 2003.

[3] S. C. Ng, E. Y. K. Fok, "A framework for early discovery of breast tumor using thermography with artificial neural network," *Breast J.*, vol. 9, pp. 341–343, 2003.

[4] H. R. Dirk Grosenick, K. Thomas Moesta, Heidrun Wabnitz, Jörg Mucke, Christian Stroszczynski, Rainer Macdonald, Peter M. Schlag, "Time domain optical mammography: Initial clinical results on detection and characterization of breast tumors," *Appl. Opt.*, vol. 42, no. 16, pp. 3170–3186, 2003.

[5] E. Y. K. Ng, S. V. Sree, K. H. Ng, and G. Kaw, "The use of tissue electrical characteristics for breast cancer detection: a perspective review.," *Technol. Cancer Res. Treat.*, vol. 7, no. 4, pp. 295–308, Aug. 2008.

[6] A. H. Israyelyan, "The Development Of Molecular Diagnostics For Breast Cancer," Louisiana State University, 2003.

[7] C. A. Gonzalez, L. M. Lozano, M. C. Uscanga, J. G. Silva, and S. M. Polo, "Theoretical and Experimental Estimations of Volumetric Inductive Phase Shift in Breast Cancer Tissue," *J. Phys. Conf. Ser.*, vol. 434, p. 012004 (4 pp.), 2013.

[8] C. A. González, "Simulation of Multi-Frequency Induced Currents in Biophysical Models and Agar Phantoms of Breast Cancer," *J. Electromagn. Anal. Appl.*, vol. 04, no. 08, pp. 317–325, 2012.

[9] Z. Zakaria, R. A. Rahim, M. S. B. Mansor, S. Yaacob, N. M. N. Ayob, S. Z. M. Muji, M. H. F. Rahiman, and S. M. K. S. Aman, "Advancements in transmitters and sensors for biological tissue imaging in Magnetic Induction Tomography," *Sensors (Switzerland)*, vol. 12, no. 6, pp. 7126–7156, 2012.

[10] F. A. Duck, *Physical properties of tissue*. Academic Press Limited (London NW1), 1990.

[11] J. Tang, C. Deng, and G. B. Huang, "Extreme Learning Machine for Multilayer Perceptron," *IEEE Trans. Neural Networks Learn. Syst.*, pp. 1–13, 2015.

[12] K. Ö. Özkan and N. G. Gençer, "Low-frequency magnetic subsurface imaging: Reconstructing conductivity images of biological tissues via magnetic measurements," *IEEE Trans. Med. Imaging*, vol. 28, no. 4, pp. 564–570, 2009.

[13] I. Marinova and V. Mateev, "Determination of Electromagnetic Properties of Human Tissues," vol. 4, no. 6, pp. 733–737, 2010.

[14] A. Barai, S. Watson, H. Griffiths, and R. Patz, "Magnetic induction spectroscopy: non-contact measurement of the electrical conductivity spectra of biological samples," *Meas. Sci. Technol.*,

vol. 23, no. 8, p. 085501, 2012.

[15] Y. Wan, M. Negishi, and R. T. Constable, "A feasibility study of magnetic resonance driven electrical impedance tomography using a phantom.," *Physiol. Meas.*, vol. 34, no. 6, pp. 623–44, 2013.

[16] C. A. Gonzales and B. Rubinsky, "Frequency Dependence of Phase Shift in Edema: a Theoritical Study with Magnetic Induction," *Proc. 2005 IEEE Eng. Med. Biol. 27th Annu. Conf.*, pp. 3518–3521, 2005.

[17] C. A. Gonzalez, R. Rojas, C. Villanueva, and B. Rubinsky, "Inductive phase shift spectroscopy for volumetric brain edema detection: An experimental simulation," *Annu. Int. Conf. IEEE Eng. Med. Biol. - Proc.*, pp. 2346–2349, 2007.

[18] C. A. Gonzalez, J. A. Valencia, A. Mora, F. Gonzalez, B. Velasco, M. a. Porras, J. Salgado, S. M. Polo, N. Hevia-Montiel, S. Cordero, and B. Rubinsky, "Volumetric Electromagnetic Phase-Shift Spectroscopy of Brain Edema and Hematoma," *PLoS One*, vol. 8, no. 5, pp. 1–10, 2013.

[19] J. Sun, G. Jin, M. X. Qin, Z. B. Wan, J. B. Wang, C. Wang, W. Y. Guo, L. Xu, X. Ning, J. Xu, X. J. Pu, M. S. Chen, and H. M. Zhao, "Detection of acute cerebral hemorrhage in rabbits by magnetic induction," *Braz J Med Biol Res*, vol. 47, no. 2, pp. 144–150, 2014.

[20] W. Pan, Q. Yan, M. Qin, G. Jin, J. Sun, X. Ning, W. Zhuang, B. Peng, and G. Li, "Detection of cerebral hemorrhage in rabbits by time-difference magnetic inductive phase shift spectroscopy," *PLoS One*, vol. 10, no. 5, pp. 1–14, 2015.

[21] C. A. González, C. Villanueva, C. Vera, O. Flores, R. D. Reyes, and B. Rubinsky, "The detection of brain ischaemia in rats by inductive phase shift spectroscopy.," *Physiol. Meas.*, vol. 30, no. 8, pp. 809–819, 2009.

[22] B. Gowry, A.B. Shahriman, Z. Zakaria, R. Ikeura, M.R. Zuradzman, D. Hazry, W.A. Wan Khairunizam, E.M. Cheng (In press), "Inductive Phase Shift As A Future Cost Effective Diagnostic Tool In Breast Cancer Localization: A Prologue Study," in *International Conference On Advanced Science, Engineering And Technology (ICASET 2015)*.

[23] S. A. Alshehri and S. Khatun, "UWB imaging for breast cancer detection using neural network," *Prog. Electromagn. Res. C*, vol. 7, pp. 79–93, 2009.

[24] A. Miraoui, L. Merad, S. Meriah, "Microwave Imaging For The Detection And Localization Of Breast Cancer Using Artificial," *Journal of Theoretical and Applied Information Technology*, vol. 74, no. 3, pp. 329–335, 2015.

[25] K. R. Foster, H. P. Schwan, "Dielectric properties of tissues and biological materials: a critical review," *CRC Crit Rev Biomed Eng*, vol. 7, pp. 25–104, 1989.

[26] L. Ma, "Magnetic Induction Tomography for Non-destructive Evaluation and Process Tomography," University of Bath, 2014.

[27] Q. Marashdeh and F. L. Teixeira, "Sensitivity matrix calculation for fast 3-D electrical capacitance tomography (ECT) of flow systems," *IEEE Trans. Magn.*, vol. 40, no. 2, pp. 1204–1207, 2004.

[28] M. Soleimani and W. R. B. Lionheart, "Image reconstruction in three-dimensional magnetostatic permeability tomography," *IEEE Trans. Magn.*, vol. 41, no. 4, pp. 1274–1279, 2005.

[29] M. Soleimani and K. Willuhn, "Sensitivity analysis for magnetic induction tomography.," *Conf. Proc. ... Annu. Int. Conf. IEEE Eng. Med. Biol. Soc. IEEE Eng. Med. Biol. Soc. Annu. Conf.*, vol. 2, pp. 1368–71, 2004.

[30] Zulkarnay Zakaria, "Magnetic Induction Tomography for Imaging of Steel in Reinforced Concrete Structure," Univerisiti Teknologi Malaysia, 2014.

[31] A. Phinyomark, P. Phukpattaranont, and C. Limsakul, "Expert Systems with Applications Feature reduction and selection for EMG signal classification," *Expert Syst. Appl.*, vol. 39, no. 8, pp. 7420–7431, 2012.

[32] D. A. Clausi, "An analysis of co-occurrence texture statistics as a function of grey level quantization," *Can. J. Remote Sens.*, vol. 28, no. 1, pp. 45–62, 2002.

[33] P. Mohanaiah, P. Sathyanarayana, and L. Gurukumar, "Image Texture Feature Extraction Using GLCM Approach," *Int. J. Sci. Res. Publ.*, vol. 3, no. 5, pp. 1–5, 2013.

[34] (2015,September 16)."Extreme learning machine." [Online]. Available: https://en.wikipedia.org/wiki/Extreme_learning_machine. [Accessed: 18-Feb-2016].